

## Water Resources Research

### RESEARCH ARTICLE

10.1029/2018WR022585

#### Key Points:

- For moderate levels of hydraulic heterogeneity, fracture network structure is the principal control of transport times and dispersion
- The influence of the interplay between structural and hydraulic heterogeneity is nonlinear
- As hydraulic heterogeneity increased, both longitudinal and transverse dispersion also increased

#### Supporting Information:

- Supporting Information S1

#### Correspondence to:

J. D. Hyman,  
jhyman@lanl.gov;  
J. Jiménez-Martínez,  
joaquin.jimenez@eawag.ch,  
jjimenez@ethz.ch

#### Citation:

Hyman, J. D., & Jiménez-Martínez, J. (2018). Dispersion and mixing in three-dimensional discrete fracture networks: Nonlinear interplay between structural and hydraulic heterogeneity. *Water Resources Research*, 54, 3243–3258. <https://doi.org/10.1029/2018WR022585>

Received 17 JAN 2018

Accepted 7 APR 2018

Accepted article online 16 APR 2018

Published online 6 MAY 2018

## Dispersion and Mixing in Three-Dimensional Discrete Fracture Networks: Nonlinear Interplay Between Structural and Hydraulic Heterogeneity

J. D. Hyman<sup>1</sup>  and J. Jiménez-Martínez<sup>2,3,4</sup> 

<sup>1</sup>Computational Earth Science, Earth and Environmental Sciences Division, Los Alamos National Laboratory, Los Alamos, NM, USA, <sup>2</sup>Department Water Resources and Drinking Water, EAWAG, Dübendorf, Switzerland, <sup>3</sup>Department of Civil, Environmental and Geomatic Engineering, ETH Zurich, Zurich, Switzerland, <sup>4</sup>Earth and Environmental Sciences Division, Los Alamos National Laboratory, Los Alamos, NM, USA

**Abstract** We investigate the relative impact of topological, geometric, and hydraulic heterogeneity on transport processes in three-dimensional fracture networks. Focusing on the two largest scales of heterogeneity in these systems, individual fracture and network structure, we compare transport through analogous structured and disordered three-dimensional fracture networks with varying degrees of hydraulic heterogeneity. For the moderate levels of hydraulic heterogeneity we consider, network structure is the dominant control of transport through the networks. Less dispersion, both longitudinal and transverse, is observed in structured networks than in disordered networks, due in part to the higher connectivity in the former, independent of the level of hydraulic heterogeneity. However, increases in dispersion with higher hydraulic heterogeneity are larger in the disordered networks than in the structured networks, thereby indicating that the interplay between structural and hydraulic heterogeneity is nonlinear. We propose a measure of disorder in fracture networks by computing the Shannon entropy of the spectrum of the Laplacian of a weighted graph representation of the networks, where the weights are given by a combination of topological, geometric, and hydraulic properties. This metric, as a relative indicator by comparison between two networks, is a first approach to the dispersion potential and “mixing capacity” of a fracture network.

### 1. Introduction

Fractures and discontinuities are widespread in the subsurface in all types of rocks, and occur at different scales, ranging from micro to regional scale (Singhal & Gupta, 2010). This implies a spatial scaling of hydraulic parameters including storage coefficient and hydraulic conductivity (Jiménez-Martínez et al., 2013). In low permeability media fractures and discontinuities are the primary regions for the movement of fluids, involving processes taking place at multiple length scales (Bonnet et al., 2001). Therefore, their study is relevant for groundwater development (Roques et al., 2016), geothermal energy (Barbier, 2002), nuclear waste disposals (Cvetkovic et al., 2004), and unconventional gas production (Hyman et al., 2016b). However, while in some regions one or several families of discontinuities are well identified (e.g., Äspö Hard Rock Laboratory, Rhén, 1997), in others, the coexistence of different types of discontinuities, such as bedding planes, fractures, joints, faults and shear zones, foliation (including cleavage) or dykes, makes the definition of families difficult (e.g., Klint et al., 2004). For this reason, fractured media are usually conceptualized and classified in the literature as either regular (i.e., structured) or disordered (i.e., random) networks.

Discrete Fracture Network (DFN) models have been used since their development in 1980s (Long & Witherspoon, 1985) to conceptualize fractured media by representing each fracture individually within a network and to resolve flow and transport at different scales (Cacas et al., 1990; de Dreuzy et al., 2004, 2012; Dershowitz, 2014; Erhel et al., 2009; Hyman et al., 2015b; Ji et al., 2011; Makedonska et al., 2016; Mustapha & Mustapha, 2007; Pichot et al., 2010, 2012). The interplay between features and scales can result in flow channeling within these networks. Both the structure of a network (de Dreuzy et al., 2012; Tsang & Neretnieks, 1998) and the spatial variability of aperture within a single fracture (Johnson et al., 2006; Moreno et al., 1988; Tsang & Tsang, 1989) can create preferential flow regions. The topology of the network also results in variable flow field within fractures even when an assumption of uniform aperture is adopted (Hyman et al.,

2015b; Makedonska et al., 2016). de Dreuzy et al. (de Dreuzy et al., 2012), using DFN, studied the combined effect of fracture scale heterogeneity (i.e., distribution of local apertures) and network topology (i.e., fracture length distribution and density) on the flow properties, showing that there is a significant coupling between flow heterogeneities at the fracture scale and at the network scale. However, when the system size is sufficiently larger than the correlation length, this coupling is found to be weak. Therefore, fracture apertures, length and density distributions (de Dreuzy et al., 2012), and local roughness (Tsang & Tsang, 1989), all control flow in fractured rocks, contribute substantially to the spreading of dissolved chemicals (Tsang et al., 1996). The emergence of anomalous transport, also called non-Fickian or non-Gaussian, i.e., nonlinear scaling with time of the mean-square displacement of solute distributions (dispersion), is a direct consequence of the highly heterogeneous velocity field in this type of system (Berkowitz & Scher, 1997, 1998; Kang et al., 2015, 2017). The dynamics of fluids or solute mixing—the process that increases the actual volume occupied by the solute by smoothing out concentration contrasts (Dentz et al., 2011; Kitanidis, 1994; Ottino, 1989)—is also controlled by the structural and hydraulic heterogeneity of the network (Kang et al., 2015).

Transport processes have been studied in regular (Kang et al., 2015), commonly characterized by heterogeneity in hydraulic conductivity, and disordered (Berkowitz & Scher, 1997, 1998; Kang et al., 2017) fracture networks. The impact of interplay between network heterogeneity and heterogeneity in hydraulic conductivity on solute dispersion and mixing is still an open question that requires a three-dimensional fracture network model capable of resolving the multiple length scales within a fracture network. The smallest scale in these networks is along fracture intersections/traces (quasi 1-D elements, lines). In these regions, mixing models in 2-D, e.g., streamline routing or complete mixing, have been proposed and their influence on upscaled transport behavior quantified (Kang et al., 2015). However, in 3-D, the existence of an hydraulic head distribution along the intersection allows local fluid circulation (Hyman et al., 2015a; Park et al., 2003), with a subsequent impact on fluids and solute mixing. At a slightly larger scale there are the fractures themselves (quasi 2-D elements, planes), where variable aperture, boundary conditions (i.e., locations of inflow and outflow fractures), and stress (Kang et al., 2016), can lead to flow channelization that increases fluids and solute mixing (Johnson et al., 2006). Finally there is the scale of the entire fracture network level (3-D), where the fracture orientation (Rubin & Buddemeier, 1996), density (Huseby et al., 2001), and network connectivity are the principal controls on solute dispersion and mixing.

We focus on the two largest scales (network and fracture scale) within structured and disordered three-dimensional fracture networks by simulating flow and transport through these networks with varying degrees of hydraulic heterogeneity. The structured networks are composed of square fractures drawn from three families, whose mean orientations are orthogonal to one another and are aligned with the primary Cartesian directions. The disordered networks are composed of the same sized square fractures with orientations that are uniformly random. The density and surface areas of the two networks are the same for a fair comparison. We introduce hydraulic heterogeneity by setting fracture permeabilities to be constant or drawn from log-normal distributions with variance of 0.5 and 1.0, i.e., moderate degrees of heterogeneity. We develop a measure of disorder in fracture networks that integrates topological, geometric, and hydraulic properties, the Shannon entropy of the spectrum of the Laplacian of a weighted graph representation of the networks, and which provides a first approach to the dispersion within fracture networks.

We represent the spreading of a nonreactive conservative solute by a cloud of passive tracer particles, i.e., using a Lagrangian approach. At uniformly spaced control planes we compute the longitudinal dispersion and the relative concentration of particles that cross a median plane, a proxy for transverse dispersion. The latter provides a first approach to the “mixing capacity,” but also to the reactive capacity, i.e., for fluid-fluid mixing-driven chemical reactions (fast reactions), depending on fracture network type (i.e., structured or disordered) and the hydraulic heterogeneity.

## 2. Flow and Transport Within Fracture Networks

We use dfnWorks (Hyman et al., 2015a) to generate each DFN, solve the steady state flow equations and simulate transport therein. dfnWorks combines the feature rejection algorithm for meshing FRAM (Hyman et al., 2014), the LaGrIT meshing toolbox (LaGrIT, 2013), the parallelized subsurface flow and reactive transport code PFLOTRAN (Lichtner et al., 2015), and an extension of the WALKABOUT particle tracking method (Makedonska et al., 2015; Painter et al., 2012). FRAM is used to generate the three-dimensional

fracture networks and LaGriT is used to create a conforming Delaunay triangulation of the DFN in parallel. PFLOTTRAN is used to numerically integrate the governing equations for pressure. A modification of the WALKABOUT particle tracking method is used to determine pathlines through the DFN and simulate solute transport. Details of the suite, its abilities, applications, and references for detailed implementation are provided in Hyman et al. (2015a).

## 2.1. Discrete Fracture Networks

We consider two fracture networks types. Both are composed of square fractures with sides of length 1 m in a cuboid domain of size  $25 \text{ m} \times 10 \text{ m} \times 10 \text{ m}$ . We select uniform fracture sizes to isolate the effects of network structure from influence of the distribution of fracture lengths. Fracture centers are uniformly distributed throughout the domain. A buffer region is included to remove density issues near domain boundaries. Each network is made up of three fracture families with the same target density,  $P_{32}=3 \text{ m}^{-1}$  (total fracture surface area over domain volume). Thus, the domain is relatively dense to ensure that there are several connected paths between the inflow and out flow boundaries.

Mean normal vectors of the families are aligned with the three principal axes of Cartesian space. The fracture orientations are sampled from the three-dimensional Fisher distribution,

$$f(\mathbf{x}; \boldsymbol{\mu}, \kappa) = \frac{\kappa \exp(\kappa \boldsymbol{\mu}^T \mathbf{x})}{4\pi \sinh(\kappa)}, \quad (1)$$

where  $\boldsymbol{\mu}$  is the mean direction vector ( $T$  denotes transpose), which can be expressed in terms of spherical coordinates, mean trend  $\theta$  and mean plunge  $\phi$ , and  $\kappa \geq 0$  is the concentration parameter that determines the degree of clustering around the mean direction. Values of  $\kappa$  approaching zero result in a uniform distribution of points on the sphere while larger values create points with a small deviation from mean direction. The Fisher distribution is sampled using the algorithm provided by Wood (1994).

In the first set of networks, we select a  $\kappa$  value of 20. We refer to these networks as *structured* due to the lattice like network that is obtained. Orientations in the second network are determined by taking the parameters used for the structured networks and setting  $\kappa=0.1$ , which results in uniformly random orientations. We refer to these networks as *random*. Figure 1 shows the normal vectors for fractures in a (left) structured network and in a (right) random network projected onto the unit sphere. Fractures from the same families are the same color in Figure 1 (left). Complete generation parameters for the networks are provided in Table 1.

We generate 10 independent statistically identical realizations of the structured network and 10 independent statistically identical realizations of random network. There is little variation in the upscaled properties

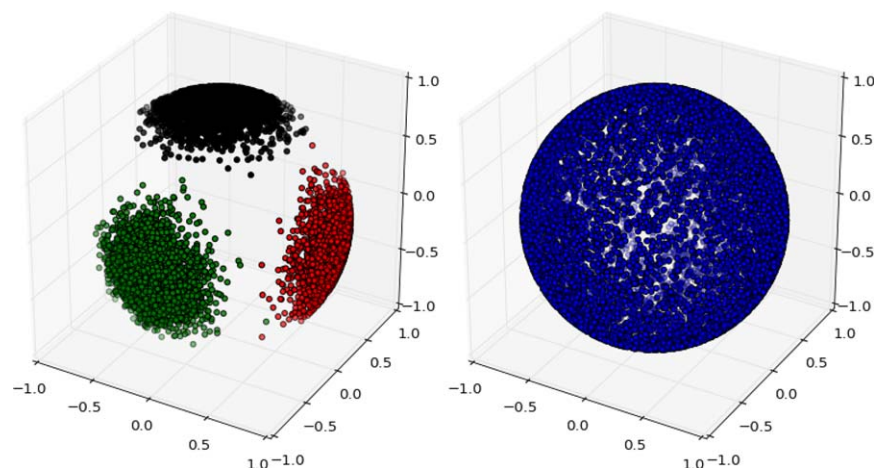


**Figure 1.** Normal vectors of the fractures in (left) a structured network and (right) a random network projected onto the surface of the unit sphere. All fracture are the same size. Colors in the structured network indicate fracture family. There are three distinct families in the structured network, each with mean orientation aligned with one of the primary Cartesian axis. There is variability around the mean sampled using a Fisher distribution. The random network has uniformly random fracture orientation.

**Table 1**  
DFN Generation Parameters

Network	Fisher distribution			Fracture density $P_{32}$
	$\Theta$	$\phi$	$\kappa$	
<i>Structured</i>				
Family 1	0	0	20	3
Family 2	$\pi/2$	0	20	3
Family 3	$\pi/2$	$\pi/2$	20	3
<i>Random</i>				
Family 1	0	0	0.1	3
Family 2	$\pi/2$	0	0.1	3
Family 3	$\pi/2$	$\pi/2$	0.1	3

Note. All networks are composed of uniform square fractures with sides of length 1 m. Parameters of the Fisher distribution for fracture orientation, equation (1): mean trend ( $\theta$ ), mean plunge ( $\phi$ ), and the concentration parameter ( $\kappa$ ). Target values of  $P_{32}$  ( $\text{m}^{-1}$ ) (total fracture surface area over domain volume).

we consider and 10 realizations is sufficient to represent statistical quantities. Examples of the variations of breakthrough curves relative to the mean behavior are provided in the supporting information. Once each network is generated, all isolated fractures are removed, which results in slight differences in final  $P_{32}$  values ( $\approx 8.75 \text{ m}^{-1}$  rather than  $9 \text{ m}^{-1}$ ). The networks both contain around 12,500 individual fractures. Each fracture is meshed with a conforming Delaunay triangulation using the feature rejection algorithm for meshing (FRAM) (Hyman et al., 2014). The minimum edge length in the mesh is 0.01 m, 100 times smaller than the fracture edge size, which was found to be sufficiently small enough to ensure that pressure and velocity solutions are not influenced by the mesh resolution (details not provided). Each fracture is meshed with around 3,000 triangles and the whole networks are meshed with around 400,000 triangles. An example of the mesh on a single fracture is provided in the supporting information. Details and theory behind the FRAM methodology are provided in Hyman et al. (2014).

We consider three different scenarios in terms of fracture permeabilities. In the baseline case, the fracture permeabilities are constant and equal between fractures ( $k=10^{-12} \text{ m}^2$ ). Apertures are determined using the cubic law and the fracture permeability. The values are physically reasonable for a 1 m fracture in crystalline rock under assumptions of a positively correlated power law relationship between fracture size and radius (Svensk Kärnbränslehantering, 2010). We consider two additional cases of hydraulic heterogeneity, in which permeabilities are sampled from log-normal distributions with log variance of  $\sigma_{\ln k}^2=0.5$  and  $\sigma_{\ln k}^2=1.0$ . The use of a lognormal distribution is motivated by the observation that conductivity values in many natural media are described by a log-normal distribution (Sanchez-Vila et al., 2006). The mean value of the distributions is equal to the value used in the constant case. The variances are chosen because they are moderate levels of hydraulic heterogeneity and are similar to those observed in crystalline rock (Svensk Kärnbränslehantering, 2010). Because all fractures are the same size, there is no correlation between fracture size and transmissivity, which is a common assumption in DFN models (Hyman et al., 2016a). Fracture permeabilities are constant within each fracture plane, in-fracture variability is not considered. Figure 2 (top) shows a structured network for the different permeability

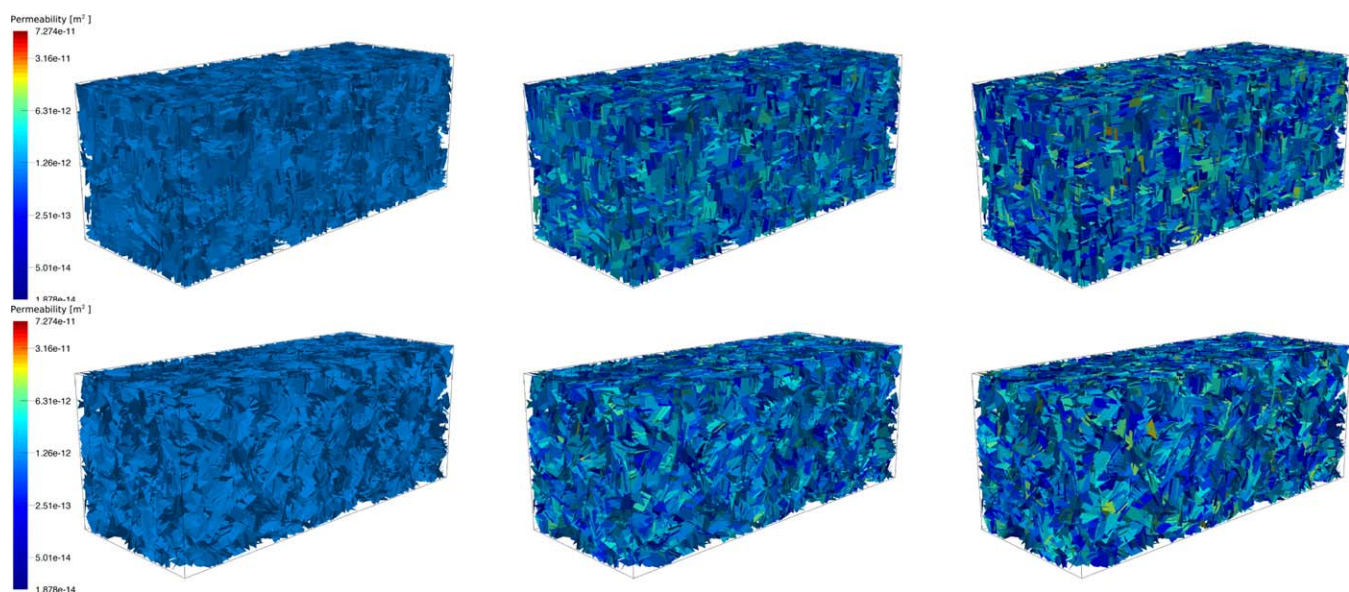


**Figure 2.** Structured (top) and random (bottom) networks with fractures colored by permeability (logarithmic scale) for permeability distributions with log variance (left)  $\sigma_{\ln k}^2=0.0$ , (middle)  $\sigma_{\ln k}^2=0.5$ , and (right)  $\sigma_{\ln k}^2=1.0$ .

distribution: (left) constant network, (middle)  $\sigma_{\ln k}^2 = 0.5$ , and (right)  $\sigma_{\ln k}^2 = 1.0$ . Fractures are colored by permeability plotted on a log scale. Figure 2 (bottom) shows the corresponding plots for one of the random network.

In total, 20 unique fracture networks are constructed. Meshing each networks takes  $\approx 2$  h (wall clock) using 32 AMD Opteron(TM) Processors 6272 (1.4 GHz). For each network, three steady state pressure fields are considered for a total of 60 flow and transport simulations. Using 64 cores obtaining steady state pressure solution requires  $\approx 1.5$  h (wall clock) for the constant permeability case. As  $\sigma_{\ln k}^2$  increases the condition number of the pressure solution matrix increases as well. This results in more required CPU time for those realizations (up to 24 h for a single run), primarily due to i/o associated with saving Lagrangian information.

## 2.2. Flow Equations

In the DFN methodology, the matrix surrounding the fractures is impervious and there is no interaction between flow within the fractures and the solid matrix. Within each fracture the flow of a Newtonian fluid, in our case water, at low Reynolds numbers is governed by the Darcy equation

$$\mathbf{q} = -\frac{\mathbf{K}}{\mu} \nabla P, \quad (2)$$

where  $\mathbf{q}$  is the Darcy flow rate,  $\nabla P$  is the pressure gradient,  $\mu$  is the fluid viscosity, and  $\mathbf{K}$  is the fracture permeability tensor, which we take to be a scalar  $\mathbf{K} = k$ . We drive flow through the domain by applying a pressure difference of 1 MPa across the domain along the  $x$  axis. No-flow boundary conditions are applied along lateral boundaries. For simplicity, the effects of gravity are not considered in these simulations. Mass conservation along with equation (2) are used to form an elliptic partial differential equation for the steady state distribution of pressure within the network

$$\nabla \cdot (k(\mathbf{x}) \nabla P) = 0. \quad (3)$$

Equation (3) is numerically integrated using a two-point flux finite-volume scheme implemented in PFLOTRAN that ensures local mass conservation within fracture planes and at fracture intersections.

While  $k$  is uniform in each fracture plane, it does vary between fractures for cases with  $\sigma_{\ln k}^2 > 0.0$ . This variability between fractures is another degree of heterogeneity in the system, in addition to the structural differences between the two networks, that affects the pressure solution and in turn fluid velocity and solute transport. Figure 3 shows the steady state pressure solution in a structured network (left) and a random network (right) for  $\sigma_{\ln k}^2 = 1.0$ .

The pressure values at cell centers and volumetric flow rates across cell boundaries returned by PFLOTRAN are used to determine the velocity field  $\mathbf{u}$  at every node in the conforming Delaunay triangulation throughout each domain using the methods of Painter et al. (2012) and Makedonska et al. (2015). Complete mixing, where the probability of a particle exiting in a given direction is proportional to the outgoing flux in that direction, is adopted at fracture intersections (Makedonska et al., 2015).

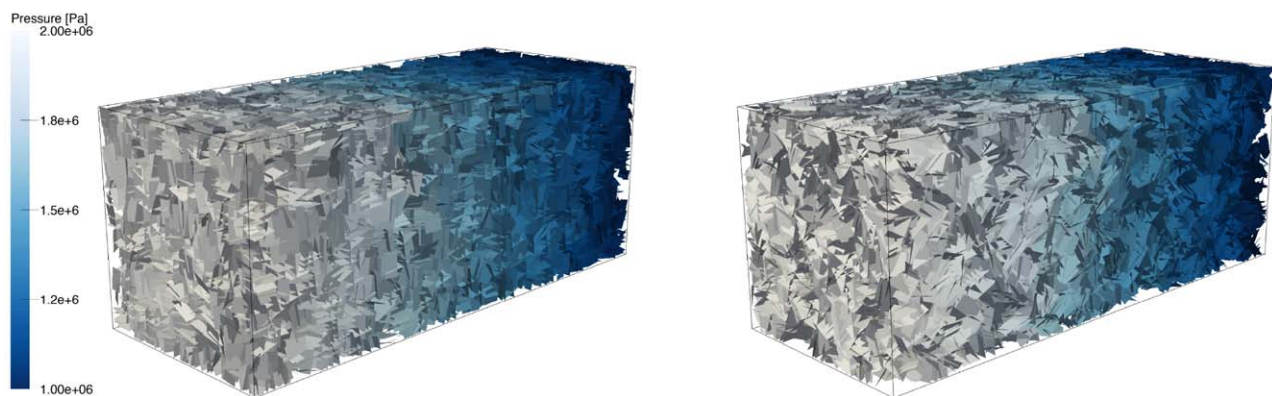


**Figure 3.** Steady state pressure solution in (left) a structured network and (right) a random network, both permeability distributions with log variance of  $\sigma_{\ln k}^2 = 1.0$ .

### 2.3. Transport Simulations

We represent the spreading of a purely advective nonreactive solute through each DFN by a cloud of indivisible passive tracer particles, i.e., using a Lagrangian approach. The use of particle tracking methods allows for the investigation of direct links between transport properties and the network structure while mitigating issues of numerical dispersion associated with Eulerian transport simulations. One hundred thousand particles are tracked through each network. In total over 6 million particle pathlines are determined and analyzed. Preliminary studies showed that upscaled quantities of interest were insensitive to including more particles (details not included). Matrix diffusion is not included in these simulations because we seek to investigate the relative importance of network structure and hydraulic heterogeneity, which is easier to quantify in the absence of matrix diffusion. Thus, the model and analysis is limited to situations where the times are too short enough to allow diffusion into the rock matrix or in the case of a very low permeability rock matrix.

Let  $\Omega$  denote the set of particles with initial positions  $\mathbf{x}_0$ . Given a fixed mass  $M$  represented by  $\Omega$  and total area of fractures along the inlet plane  $A$ , the mass associated with each particle,  $m(\mathbf{x}_0)$ , is distributed across all the particles according to

$$m(\mathbf{x}_0) = \frac{Q(\mathbf{x}_0) M}{Q A}, \quad (4)$$

where  $Q(\mathbf{x}_0)$  is the local flux rate at the initial position and  $Q$  is the total flux into the domain. This initial condition is referred to flux-weighted injection, as opposed to resident or uniform (Kreft and Zuber, 1978). These two initial conditions represent different physical scenarios and have been studied in both heterogeneous porous media and fracture networks (Demmy et al., 1999; Frampton & Cvetkovic, 2009; Gotovac et al., 2010, 2009; Hyman et al., 2015b; Janković & Fiori, 2010; Vanderborght et al., 1998; Kang et al., 2017). The choice of flux-weighted is born from wanting to observe how the system behaves at equilibrium, the equidistant sampled Lagrangian velocity distributions along are stationary for flux-injection and equal to the Eulerian velocity pdf so long as the fields are stationary and ergodic (Comolli & Dentz, 2017; Dentz et al., 2016). One could use resident (uniform) injection, having the same mass (number of particles) per unit of fracture length at the inlet plane, so that variability in the concentration profile along the inlet plane depends solely on network structure, not flux profile. In this case, one can observe the evolution of the particle plume into the stationary Lagrangian velocity distributions.

#### 2.3.1. Particle Trajectories

Particles are released at unique points along the fractures that intersect the inlet plane of the domain at  $x = 0$  at time  $t = 0$ . The trajectory  $\mathbf{x}(t; \mathbf{x}_0)$  of the particle starting at  $\mathbf{x}_0 = (0, y, z)$  is given by

$$\frac{d\mathbf{x}(t; \mathbf{x}_0)}{dt} = \mathbf{v}(t; \mathbf{x}_0), \quad \mathbf{x}(0; \mathbf{x}_0) = \mathbf{x}_0, \quad (5)$$

where the Lagrangian velocity  $\mathbf{v}(t; \mathbf{x}_0)$  is given in terms of the Eulerian velocity  $\mathbf{u}(\mathbf{x})$  as

$$\mathbf{v}(t; \mathbf{x}_0) = \mathbf{u}[\mathbf{x}(t; \mathbf{x}_0)]. \quad (6)$$

The length of the pathline,  $\ell$ , is used to parameterize the spatial and temporal coordinates of the particle. The space-time particle trajectory is given in terms of  $\ell$  by

$$\frac{d\mathbf{x}(\ell; \mathbf{x}_0)}{d\ell} = \frac{\mathbf{v}[t(\ell); \mathbf{x}_0]}{v[t(\ell); \mathbf{x}_0]}, \quad (7a)$$

$$\frac{dt(\ell; \mathbf{x}_0)}{d\ell} = \frac{1}{v[t(\ell), \mathbf{x}_0]}, \quad (7b)$$

where we set  $v(t, \mathbf{x}_0) = |\mathbf{v}(t; \mathbf{x}_0)|$ . The length  $\ell(t; \mathbf{x}_0)$  of the trajectory at a time  $t$  is given by

$$\frac{d\ell(t; \mathbf{x}_0)}{dt} = v_\ell[\ell(t), \mathbf{x}_0], \quad (8)$$

where we defined  $v_\ell(\ell; \mathbf{x}_0) = v[t(\ell); \mathbf{x}_0]$ .

The arrival time  $\tau(x'; \mathbf{x}_0)$  of a particle at a control plane perpendicular to the primary direction of flow and at distance  $x'$  from the inlet is given by

$$\tau(x'; \mathbf{x}_0) = t[\lambda(x'); \mathbf{x}_0], \quad \lambda(x) = \inf \{ \ell | x(\ell; \mathbf{x}_0) \geq x' \}. \quad (9)$$

### 2.3.2. Breakthrough Times

The mass represented by a particle and the breakthrough time at a control plane can be combined to compute the total solute mass flux  $\Psi(t, x')$  that has broken through a control plane at  $x'$  at time  $t$ ,

$$\Psi(t, x') = \frac{1}{M} \int d\Omega \, m(\mathbf{x}_0) H[t - \tau(x', \mathbf{x}_0)]. \quad (10)$$

Here  $H(t)$  is the Heavyside function where  $H(t) = 1$  for  $t > 0$ , and  $H(t) = 0$  otherwise. Equation (10) is the integral form of the cumulative distribution function (CDF) of solute passing through a control plane. We also consider the complementary cumulative distribution function (CCDF)  $1 - \Psi(t, x)$ , which when plotted on a log-log scale can be used to determine power law scaling of the tail of the  $\Psi(t, x)$ . The relevant solute flux through this control plane is

$$\psi(t, x') = \frac{d\Psi(t, x')}{dt} = \frac{1}{M} \int d\Omega \, m(\mathbf{x}_0) \delta[t - \tau(x', \mathbf{x}_0)], \quad (11)$$

which is an integral form of the breakthrough curve. Placing (4) into (11) one obtains the distributions of travel time for our adopted initial conditions:

$$\psi(t, x') = \frac{1}{AQ} \int d\Omega \, Q(\mathbf{x}_0) \delta[t - \tau(x', \mathbf{x}_0)]. \quad (12)$$

We consider control planes with spacing  $\Delta x = 1$  m, the fracture size.

### 2.3.3. Dispersion Quantification

At each control plane we compute the mean squared displacement of the particle plume travel times,

$$\sigma_t^2(x') = \frac{1}{AQ} \int d\Omega \, Q(\mathbf{x}_0) [\tau(x', \mathbf{x}_0) - \overline{\tau(x')}]^2, \quad (13)$$

where overbar indicates average over all particles in a plume. We focus on spreading in the majority of the plume by limiting (13) to the initial 99.9% of the mass that breaks through the control plane. We also investigate the tailing behavior using a different set of tools; those mentioned above. Taking the derivative of (13) with respect to the primary direction of flow  $\partial \sigma_t^2(x') / \partial x$ , quantifies the stability of the plume as it moves through the domain. If the bulk of the plume is relatively stable, then the values of  $\partial \sigma_t^2(x') / \partial x \ll 1$ , otherwise the plume is still growing.

The movement of mass transverse to the primary direction of flow on the network scale is quantified by computing the relative concentration of mass that crosses a plane in the center of the domain parallel to the primary direction of flow. We provide an analysis for the median plane aligned with  $y = 0$ , but similar results are obtained when performing the same analysis using a plane at  $z = 0$ . First, we divide the set of all pathlines ( $\Omega$ ) into two disjoint sets. The set  $A$  contains all pathlines whose initial  $y$  coordinate, denoted  $\mathbf{x}_0^i(y)$ , is less than zero and the set  $B$  contains all pathlines whose initial  $y$  coordinate is greater than or equal to zero,

$$A = \{i : \mathbf{x}_0^i(y) < 0\} \text{ and } B = \{i : \mathbf{x}_0^i(y) \geq 0\}, \quad (14)$$

where  $\mathbf{x}_0^i$  denotes the initial position of the  $i$ th particle. Thus,  $\Omega = A \cup B$  and  $A \cap B = \emptyset$ . The total mass traveling along all pathlines into the inlet plane is given by

$$M_0 = \int dz \int dy \int d\Omega \, m(\mathbf{x}_0). \quad (15)$$

Using this equation, we can track to the total mass transported by pathlines in  $A$  and  $B$ ,

$$\begin{aligned} M_0 &= \int dz \int dy \int d\Omega \, m(\mathbf{x}_0) \\ &= \int dz \int dy \int_{\chi_A} d\Omega \, m(\mathbf{x}_0) + \int dz \int dy \int_{\chi_B} d\Omega \, m(\mathbf{x}_0) \\ &= M_A + M_B, \end{aligned} \quad (16)$$

where  $\chi_A$  is the indicator function for pathlines in  $A$  and  $\chi_B$  is the indicator function for pathlines in  $B$ . At a control plane at distance  $x'$  from the inlet plane, we can compute the amount of mass traveling along pathlines in  $A$  that has crossed the median  $y$  plane using

$$M_A^+(x') = \int dz \int_{y \geq 0} dy \int_{\Omega_A} d\Omega m(x', y, z). \quad (17)$$

Likewise, the mass traveling along pathlines in  $B$  that has crossed the median  $y$  plane is

$$M_B^-(x') = \int dz \int_{y < 0} dy \int_{\Omega_B} d\Omega m(x', y, z). \quad (18)$$

The relative mass that has crossed the median at each control plane is given by

$$M^*(x') = \frac{M_A^+(x') + M_B^-(x')}{M_0}. \quad (19)$$

### 3. Simulation Results

In this section, we first report structural (topological and geometric) and hydraulic attributes of the fracture networks. Then, we report observations of flow velocities and transport through them.

#### 3.1. Network Structure

The fracture network sets, structured, and random, exhibit different topological properties, which result from the different family structures. We quantify their differences by considering two topological properties, one local and one global. Topological characterization is performed by constructing a graph representation of each network using the method described in Hyman et al. (2017). For each fracture in the DFN, there is a unique node in a graph. If two fractures intersect, then there is an edge in the graph connecting the corresponding nodes. Edges are assigned unit weight to isolate topological attributes from other attributes that could be considered. All fractures that intersect the inflow plane are connected to a source node and all fractures that intersect the outflow plane are connected to a target node. Thus, the graphs are based solely on the topology (connectivity) of the networks. We use the NetworkX graph software package (Hagberg et al., 2008) to compute topological properties of interest of the graphs.

The local attribute we consider is the number of other fractures that each fracture intersects (i.e., local topological heterogeneity), which we refer to as the *fracture degree*. The distribution of these values for both types of networks (i.e., structured and random) is provided in Figure 4. The integer median of these distributions is 4 for the structured network and 3 for the random network. Thus, a typical fracture in the structured network connects to four other fractures while a typical fracture in the random network only connects to three others. Moreover, the distribution of the structured network has higher variance (2.64) than the random one (1.98). These values indicate that the structured network is slightly better connected locally than the random network.

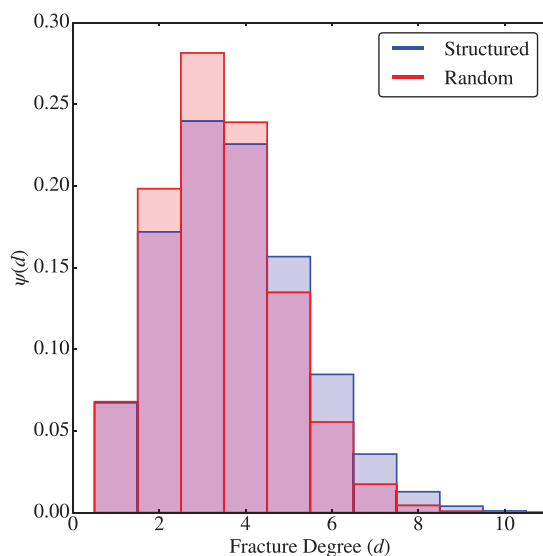


**Figure 4.** Distribution of fracture connectivity (*fracture degree*) for the structured networks (blue) and the random networks (red).

The global (i.e., network-scale heterogeneity) property considered is the *node connectivity* of the networks, which is the number of nodes (fractures) that need to be removed to disconnect the inflow and boundaries. This value indicates how well a network is connected with respect to the flow boundaries. The higher the value, the more difficult it is to disconnect the inflow and outflow boundaries. The average node connectivity is 71.9 (variance of 8.09) for the structured and 57.5 (variance of 6.25) for the random network. These values indicate that the structured network is globally better connected than the random network.

Although each fracture is the same shape, a range of length scales exists within the fracture plane due to intersections among fractures. A first order approximation of the transport distances within the fracture planes can be obtained by computing the distance between centers of intersections (traces) within fracture planes ( $l$ ). An image of this construction is shown in the supporting information. Figure 5 (left) shows the distribution of these distances for the structured (blue) and the random networks (red). The observed distribution of lengths is

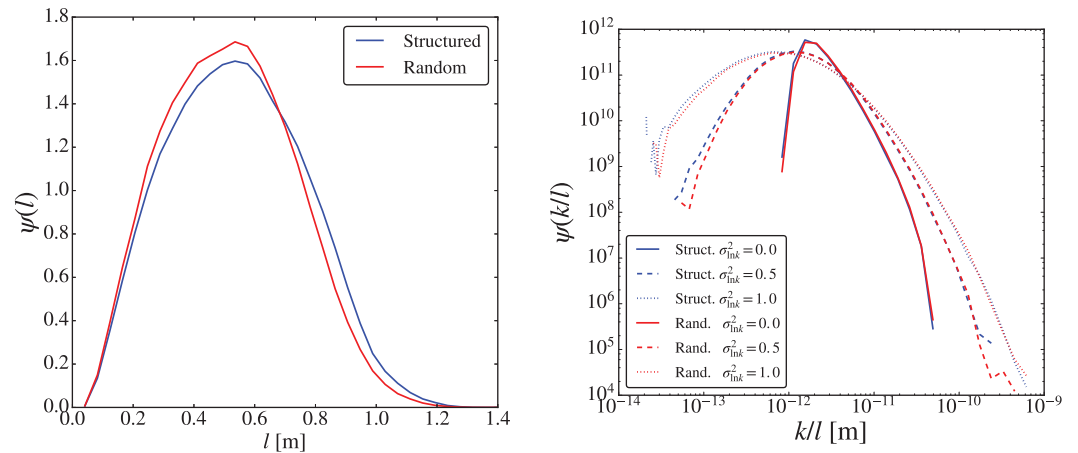


**Figure 5.** (left) In-fracture length,  $l$ , and (right) permeability/in-fracture length,  $k/l$ , distributions. Values for the structured (blue) and random (red) networks; log variance of permeability fields are distinguished by line type:  $\sigma_{\ln k}^2 = 0.0$  (solid),  $\sigma_{\ln k}^2 = 0.5$  (dashed),  $\sigma_{\ln k}^2 = 1.0$  (dotted).

quite similar, having a mean[m]±variance[m<sup>2</sup>] of  $0.52 \pm 0.049$  and  $0.49 \pm 0.044$  for the structured and random network, respectively.

Another length scale can be obtained by considering the ratio of the fracture permeability over these distances ( $l' = k/l$ ). The importance of this length scale can be seen by a change of variables within Darcy's law,

$$\mathbf{q} = -\frac{k\Delta P}{\mu l} \rightarrow \mathbf{q} = -l' \frac{\Delta P}{\mu}. \quad (20)$$

The ratio  $\Delta P/\mu$  has dimensions of 1/time, so  $\mu/\Delta P$  is a characteristic time scale of the system. Therefore,

$$l' = -\mathbf{q} \frac{\mu}{\Delta P} \quad (21)$$

is the distance traveled within a fracture plane in a characteristic time step at a given speed. Figure 5 (right) shows the distribution of  $l'$  for the structured (blue) and the random network (red) for the three cases of hydraulic variability that we consider:  $\sigma_{\ln k}^2 = 0.0$  (solid),  $\sigma_{\ln k}^2 = 0.5$  (dashed),  $\sigma_{\ln k}^2 = 1.0$  (dotted). The distributions for larger values of  $\sigma_{\ln k}^2$  have wider variance, as expected. For each value of  $\sigma_{\ln k}^2$ , the distributions of these in-plane attributes in the structured and the random networks are nearly indistinguishable. The similarity of these distributions indicates that at the scale of individual fractures the two networks are analogous.

We combine topological, geometric, and hydraulic properties to examine the interplay between structural and hydraulic heterogeneity with respect to their influence on transport properties through the fracture networks. Specifically, we compute the *Shannon entropy* for each of the networks as a measure of how easily particles can move through the networks. For this computation, we use a different graph representation of each DFN than that used above. To better include more geometric and hydraulic information, nodes in the graph represent intersections between two fractures and edges represent paths between traces along a fracture plane. This mapping allows for geometric and hydraulic properties to be represented as edge weights in the graph. Details of the mapping are included in the supporting information. This mapping is similar to those used in pipe-network flow simulations within DFN, e.g., Dershowitz and Fidelibus (1999). Weights are based on the length between intersections and permeability. We use an unnormalized linear weighting scheme where the edge weight is permeability of the fracture over the distance between trace centroids  $w = l' = k/l$ . Using this weighted graph representation, we determine the spectrum of the normalized graph Laplacian, and then compute the Shannon entropy of this as:  $E = -\sum_{i=1}^n p(c_i) \log p(c_i)$ , where  $p(c_i)$  is the eigenvalue probability distribution of the largest 200 normalized eigenvalues, i.e., the probability of defining an edge in the network with eigenvalue or relative importance  $c_i$  (Jiménez-Martínez & Negre, 2017). The size of the Laplacian  $\mathcal{O}(20,000) \times \mathcal{O}(20,000)$  prohibited obtaining the entire spectrum. Average values of the Shannon entropy for all networks along with variances are provided in Table 2.

**Table 2**  
Shannon Entropy for the Structured and Random Fracture Networks

Weights	Structured		Random	
	Mean	Variance	Mean	Variance
$\sigma_{lnk}^2 = 0.0$	11.36	0.64	11.79	0.70
$\sigma_{lnk}^2 = 0.5$	12.43	0.37	13.40	0.44
$\sigma_{lnk}^2 = 1.0$	13.41	0.41	14.77	0.40

Note. Entropy is computed using largest 200 normalized eigenvalues of the spectrum of the weighted graph Laplacian with weights based on  $k/l$  (m).

### 3.2. Velocity Distributions

Figure 6 shows the average distribution of Eulerian velocity magnitudes ( $\|\mathbf{u}(\mathbf{x})\|$ ) in the structured networks and the random networks for all three hydraulic cases. The random networks have more low velocity regions than the structured networks. Low flow velocities are more common with higher values of  $\sigma_{lnk}^2$  in both network structures.

### 3.3. Particle Transport

The influence of these low velocity regions is apparent in the breakthrough times at the outlet plane,  $L = 25$  m (Figure 7). Figure 7 (left) shows the distributions of breakthrough times computed using equation (12). All curves, here and in subsequent images, show the average

of each network set for each value of  $\sigma_{lnk}^2$ . Examples of the variations of breakthrough curves for individual realizations relative to the mean behavior are provided in the supporting information. Times have been nondimensionalized by the median breakthrough time of particles through the structured network with constant permeability ( $\sigma_{lnk}^2 = 0.0$ ). The peak breakthrough is lower and later for the random than the structured network for all three  $\sigma_{lnk}^2$  cases. Figure 7 (right) shows the complementary cumulative distributions of breakthrough times computed using equation (10). Later breakthrough times are observed in the random networks than their structured counterparts. As hydraulic heterogeneity increases, later breakthrough times are observed in both network structures.

The evolution of plume spreading in the primary direction of flow is quantified by computing the mean squared displacement  $\sigma_x^2$  via equation (13) at equidistant control planes ( $\Delta x = 1$  m). The derivative of  $\sigma_x^2$  with respect to primary flow direction,  $\partial \sigma_x^2(x') / \partial x$ , is shown in Figure 8, where colors and line style are the same as in Figure 7, to highlight plume growth rates. Beyond the first control plane, the values of  $\partial \sigma_x^2(x') / \partial x$  are somewhat constant, i.e.,  $\sigma_x^2$  increases roughly linearly, as the plume moves through subsequent control planes for all cases. There does, however, appear to be some boundary influence near the inlet and outlet regions. The random networks have consistently higher values of  $\partial \sigma_x^2(x') / \partial x$  than the structured networks for the same value of  $\sigma_{lnk}^2$ , indicating faster growth of the plume. Higher values of  $\sigma_{lnk}^2$  result in higher values of  $\partial \sigma_x^2(x') / \partial x$  in both network structures. The differences between  $\partial \sigma_x^2(x') / \partial x$  values for increasing values of  $\sigma_{lnk}^2$  are larger for the random than the structured networks.

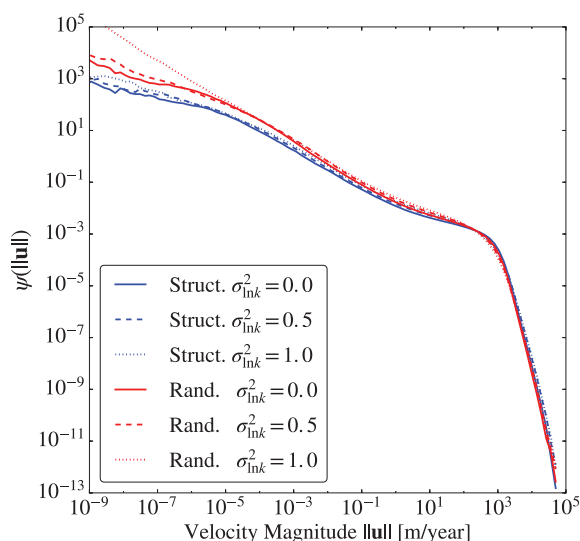


**Figure 6.** Distribution of velocity magnitudes in the structured (blue) and the random (red) network. Log variance of permeability fields are distinguished by line type:  $\sigma_{lnk}^2 = 0.0$  (solid),  $\sigma_{lnk}^2 = 0.5$  (dashed),  $\sigma_{lnk}^2 = 1.0$  (dotted).

Particles also disperse through the network in directions transverse to the primary direction of flow. Figure 9 shows 100 particle pathlines in the randomly oriented network with  $\sigma_{lnk}^2 = 1.0$ . The pathlines are colored according to particle initial positions. Particles starting on the left side of the domain are colored blue and those starting on the right are colored red. Along with the pathlines, uniformly spaced control planes normal to the main flow direction are also included (see also left side of the image). As particles move through the domain, they transition across this median plane, i.e., transverse movement occurs within the network. By the end of the domain, particles are mixed with respect to their origin. Equation (19) measures the relative mass that has transitioned across the median plane with distance traveled. Observations for all networks are provided in Figure 10. Distributions of particle locations used to compute these values are provided in the supporting information. A consistent increase in values of the relative concentration is observed, with larger values for the random than for the structured network. For the same network structure, there is little difference in the observed values between  $\sigma_{lnk}^2 = 0.0$  and  $\sigma_{lnk}^2 = 0.5$ , while for  $\sigma_{lnk}^2 = 1.0$ , there is a noticeable power law scaling with distance traveled,  $M^*(x) = \beta x^2$ , although the limited length of the domain is not sufficient to confirm this hypothesis.

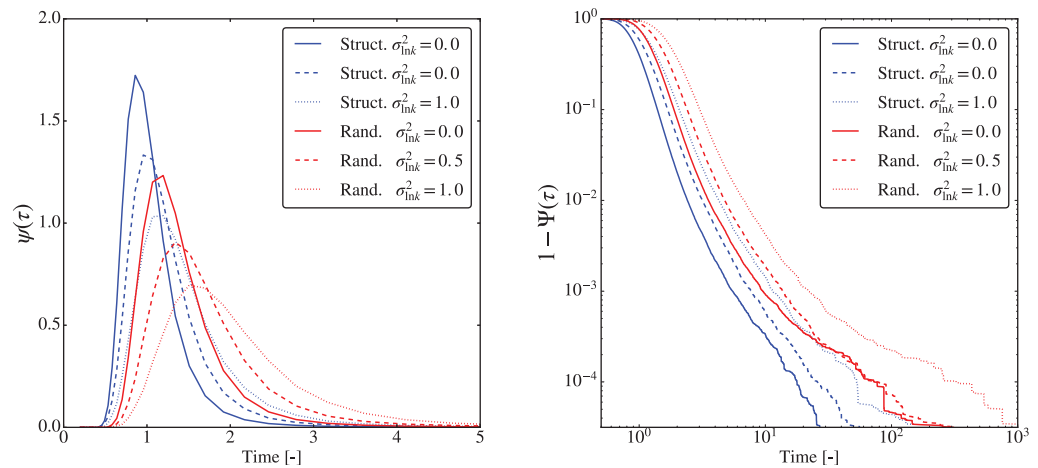


**Figure 7.** Breakthrough times at the outlet plane ( $L = 25$  m) for structured (blue) and random (red) networks. Log variance of permeability fields are distinguished by line type:  $\sigma_{lnk}^2 = 0.0$  (solid),  $\sigma_{lnk}^2 = 0.5$  (dashed),  $\sigma_{lnk}^2 = 1.0$  (dotted). Times are non-dimensionalized by the median breakthrough time of structured network with log variance  $\sigma_{lnk}^2 = 0.0$ . (left) Distributions of breakthrough times computed using equation (12). (right) Complementary cumulative distributions of breakthrough times computed using equation (10).

## 4. Discussion

By a number of measures, the two fracture network sets studied, structured and random, are very similar. This, along with the same boundary and initial conditions, allows for a systematic and quantitative comparison between them, as well as an opportunity to address the impact of the interplay between structural and hydraulic heterogeneity on solute dispersion and mixing.

### 4.1. Structural Control

Differences in transport behavior within the two networks for the same value of  $\sigma_{lnk}^2$  are the result of differences in their network-scale (i.e., macroscale) structure. This conclusion is supported by the following observations. First, the networks were designed to be analogous at the scale of individual fractures. They are composed of equal-sized fractures whose centroids are uniformly distributed throughout the domain and have similar values of total fracture surface area (over domain volume) and density (Table 1). Second, their hydraulic properties are statistically indistinguishable, having either the same permeabilities on every fracture or fracture permeabilities drawn from the same distribution. Distributions of distances between trace centroids are similar (Figure 5 (left)) and the distributions of the length scale  $l'$  (ratio of permeability and distance between centers of fracture plane intersections), which we proposed to establish a relationship between structural and hydraulic properties, are also nearly indistinguishable for the same values of  $\sigma_{lnk}^2$  between the networks (Figure 5 (right)).

The principal difference between the two network sets is the orientation of fracture families (Figure 1). In the structured networks, the mean orientations of the three fracture families are orthogonal to one another and are aligned with the primary Cartesian directions. Therefore, two of the three families in the structured networks contain fractures that are aligned with the principal direction of flow and provide little resistance to flow and transport. In contrast, the disordered networks are composed of square fractures of the same size, but whose orientations are uniformly random and provide no preferred direction or resistance to flow. This difference between orientations also resulted in networks with different connectivity properties. The two measures proposed for connectivity, fracture degree and node connectivity, indicate that the structured networks are better connected,

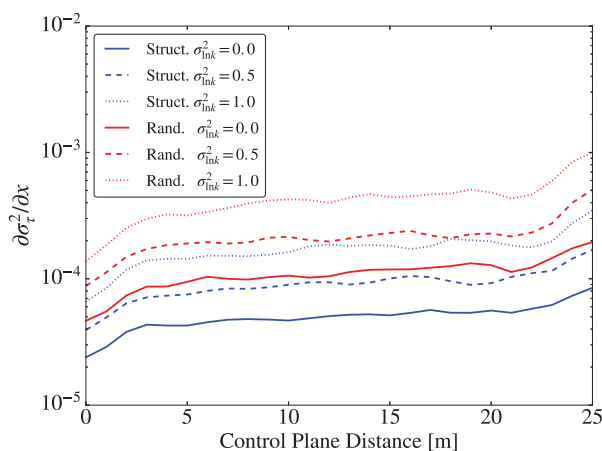


**Figure 8.** Derivative of mean squared displacement  $\sigma_{\tau}^2$  of breakthrough times respect to the primary direction of flow (plume growth rate).  $\partial\sigma_{\tau}^2(x')/\partial x$  plotted as a function of control plane distance for structured (blue) and random (red) network. Log variance of permeability fields are distinguished by line type:  $\sigma_{lnk}^2 = 0.0$  (solid),  $\sigma_{lnk}^2 = 0.5$  (dashed),  $\sigma_{lnk}^2 = 1.0$  (dotted).

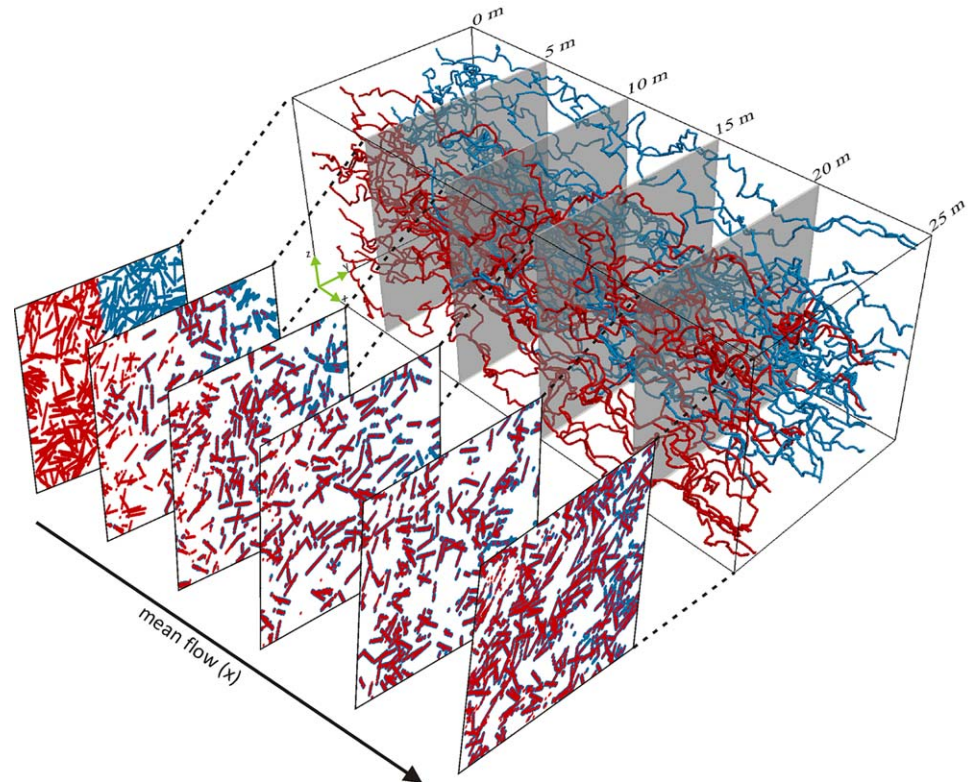


**Figure 9.** Pathlines of 100 particles in the random network with  $\sigma_{lnk}^2 = 1.0$ . The pathlines are colored according to particle initial positions: left-blue and right-red. Uniformly spaced [0–25 m] control planes (gray) normal to the main flow direction are also included. The left side of the image shows snapshots of particle locations at the normal control planes. As particles move through the domain, they transition across a median plane.

both locally and globally, than their random counterparts. Thus, in addition to providing less resistance in the direction of flow, it is easier for transport to pass between fractures in the structured networks.

The fracture degree (i.e., the number of fractures that each fracture intersects) corresponds to the coordination value—a global topological characteristic for the entire fractured network—in percolation theory. Karrer et al. (2014) showed that percolation threshold  $\rho_c$ —a critical probability below which the connections are too sparse

to form a pathway through a sample leading to an interrupted macroscopic flow and transport—is given by  $\rho_c = 1/(\text{fracture degree} - 1)$ . This definition of percolation threshold, originally proposed for sparse networks (tree-like networks), has been found to be accurate for denser networks (many short loops) as well (Jiménez-Martínez & Negre, 2017). The value of  $\rho_c$  was 0.333 and 0.500 for structured and random networks, respectively; while the theoretical  $\rho_c$  for 3-D systems is 0.312. The lower average fracture degree of the random network results in a percolation threshold that is similar to a well-connected 2-D system (0.590) (Berkowitz & Balberg, 1993). Although the obtained percolation threshold is subject to uncertainty, it confirms that the structured network is better connected globally.

#### 4.2. Spreading

The structured networks show a narrower distribution of velocities than the random networks for all log variance values considered. In general, the random networks display wider variance in the velocity field distribution, in which low velocities regions coexist with connected preferential paths where velocities are high. This variance is also controlled by  $\sigma_{lnk}^2$ . In contrast to 2-D DFN simulations, dead-end fractures, those with fracture degree of one, are not no-flow regions. Gradients can exist

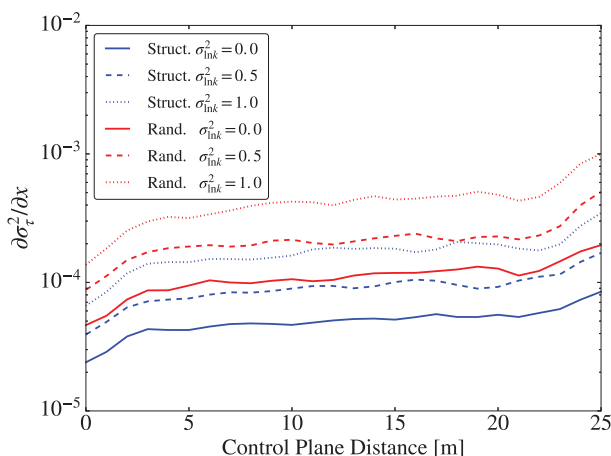


**Figure 10.** Relative concentration values  $M^*$  (equation (19)) plotted as a function of control plane distance for the structured (blue) and random (red) networks. Log variance of permeability fields are distinguished by line type:  $\sigma_{lnk}^2 = 0.0$  (solid),  $\sigma_{lnk}^2 = 0.5$  (dashed),  $\sigma_{lnk}^2 = 1.0$  (dotted).

along the single intersection on a dead-end fracture and create low velocity flow cells within the dead-end fractures. Thus, recirculation regions exist within dead-end fractures and these flow cells have been shown to contribute to delays in the particle transport, i.e., particle residence times are increased (Park et al., 2003). This effect is less pronounced in the structured networks possibly due to the higher average and wider variance of fracture degree, as well as the higher network-scale connectivity.

Higher values of  $\sigma_{\ln k}^2$  result in more longitudinal dispersion in both networks. However, the faster first arrival times in the structured networks and a lower and later breakthrough peak in the random networks for all three  $\sigma_{\ln k}^2$  cases, indicate that the greater longitudinal dispersion in the particle plume is mainly structurally controlled. Similar conclusions have recently been reached for porous media, with higher variance of the solute arrival times in spatially disordered than in more orderly conductivity fields, while in the latter, more skewed distributions, as for higher  $\sigma_{\ln k}^2$ , have been reported (Bianchi & Pedretti, 2017). Higher values of  $\sigma_{\ln k}^2$  result in higher values of  $\sigma_{\tau}^2$  in both network structures. Values of  $\partial\sigma_{\tau}^2/\partial x$  increase rapidly through the first few control planes and then stabilize to a constant until the end of the domain, which is likely the result of boundary effects. Nonetheless, the systematically higher values of  $\sigma_{\tau}^2$  for the random networks, independent of  $\sigma_{\ln k}^2$ , highlights that network structure controls macroscale dispersion. Note as well that the plot is on a semilog scale. Therefore, the systematic depends nonlinearly on  $\sigma_{\ln k}^2$  as well.

### 4.3. Transverse Dispersion: Mixing Capacity

Transverse dispersion provides a first approach to the mixing and reactive capacity of the system, i.e., for fluid-fluid mixing-driven chemical reactions (fast reactions). The relative concentration of particles crossing the median plane,  $M^*$ , measuring the transverse movement within the network, was systematically higher in the random networks (Figure 10). This indicates that structural heterogeneity plays a major role in controlling transverse dispersion (e.g., Rubin & Bddemeier, 1996), and therefore in mixing. In general, the influence of hydraulic heterogeneity is less pronounced here than in the longitudinal direction. However, for the structured network, larger transverse dispersion above a certain threshold in  $\sigma_{\ln k}^2$  (i.e.,  $\sigma_{\ln k}^2 = 1.0$ ) is observed, being heterogeneity in hydraulic properties the main control on transverse dispersion.  $M^*$ , like  $\sigma_{\tau}^2$ , increases with similar rate as the plume moves through the domain (i.e., with distance): slightly lower and increasing with  $\sigma_{\ln k}^2$  for the structured and random networks, respectively.

In 3-D fracture networks, the combination of divergence-free flow fields and gradients along fracture intersections contributes to the redistribution of the solute particles. As in porous media (e.g., Willingham et al., 2010), streamline convergence in flow-focusing zones compresses transverse concentration, while streamline divergence after flow-focusing zones expands it. This is an important mechanism for mixing diffusion-limited reactions under laminar flow conditions, as it increases the number of particles that cross the median plane, and thus the probability that they will interact with the other set of particles, i.e., mixing. Therefore, and for the similar, in the statistical sense, networks studied, the “mixing capacity”, as well as the reactivity (i.e., the quality of being or the degree to it is reactive), are mainly structurally controlled, being higher for the random than for the structured network.

Different measures to describe and quantify solute mixing in topologically complex environments, including porous and fractured media, have been proposed, among them: scalar dissipation rate, mixing degree or dilution index. Dilution index quantifies dilution as the distribution of solute mass over a medium volume, i.e., volume of the medium occupied by a solute cloud (Kitanidis, 1994). This metric is expressed as the exponential of the Shannon entropy, computed from the solute concentration probability distribution. Entropy has been marginally used to measure spatial disorder of a permeability field and its control on the flow (e.g., Journal & Deutsch, 1993]. More recently, the entropy computed from the eigenvalue probability distribution has been demonstrated to provide a measure of the “mixing capacity” of a porous medium (e.g., Jiménez-Martínez & Negre, 2017). In this work, Shannon entropy (of the spectrum of the Laplacian of a weighted graph representation of the networks) is a measure, i.e., a relative indicator by comparison between two networks, which anticipates in which network dispersion and mixing will be higher: dispersion potential and “mixing capacity”, respectively. The random networks present higher entropy values than the structured networks for all of the weighting schemes considered (Table 2). Therefore, the random networks have, a priori, a higher “mixing capacity”. Compared to the structured networks, particles experienced a greater number of heterogeneity transitions in the random networks, which promotes mixing (e.g., Bianchi & Pedretti, 2017). This connection between higher values of network entropy with higher dispersion and

mixing capacity underscores that the network structure is a dominant force controlling transport properties within fractured media.

## 5. Conclusions

Heterogeneity exists at many length scales within fractured media. We designed two synthetic network sets to isolate the influence of structure and disorder at the macroscale and then compare its importance relative to moderate levels of hydraulic heterogeneity. The networks were constructed to be analogous at the scale of individual fractures, most macroscale properties, and hydraulic properties. The random networks were designed to be a disordered network where fractures were not aligned with any preferred direction. This construction resulted in lower values of connectivity compared to a structured network, which could be linked to greater variation in transport behavior. We proposed the Shannon entropy of the fracture network, which can integrate topological, geometric, and hydraulic properties, to provide a qualitative indication of which system may show greater dispersion or mixing even though it is not sufficient to characterize transport behavior.

The primary findings of our study are the following:

1. For moderate levels of hydraulic heterogeneity, fracture network structure is the principal control on transport times and dispersion.
2. The lower mechanical dispersion observed in the structured networks appeared to be linked to the higher levels of connectivity in comparison with the poorly connected random networks.
3. As hydraulic heterogeneity increased, both longitudinal and transverse dispersion also increased.
4. The influence of the interplay between structural and hydraulic heterogeneity is nonlinear; increased hydraulic heterogeneity for the random network resulted in more dispersion than for the structured network.
5. Higher Shannon entropy of the spectrum of the normalized graph Laplacian, a measure of the disorder in the networks, was linked to greater and higher mixing capacity.

Beyond the fact that heterogeneities at different scales imply a spatial scaling of hydraulic parameters (i.e., storage coefficient and hydraulic conductivity), the noninclusion of some heterogeneity families could suppose changing from a random to a structural network, with the subsequent implications for transport and mixing as shown in this work. Therefore, geological characterization (planes) at all scales (from foliation to large-scale fractures), including work in the laboratory (e.g., cores) and field (e.g., well logs, cartography), are essential to propose an equivalent system from DFN. Below the scale of individual fractures there are further levels of heterogeneity to consider, e.g., in-fracture aperture variability and mixing rules along intersects. Also, this study assumed that the matrix surrounding the fractures was impervious. Therefore, our model is limited to situations where the times are too short enough to allow diffusion into the rock matrix or very low permeability rock matrix. The influence of these features will be the focus of subsequent studies.

## Acknowledgments

JDH acknowledges the support of LANL LDRD Director's Postdoctoral Fellowship grant 20150763PRD4, LANL LDRD-DR grant 20170103DR and DOE's Office of Science Basic Energy Sciences E3W1. We thank D. O'Malley and M. Dentz for the fruitful and constructive discussions and Daniel Fernández-García for handling the manuscript as the Associate Editor. The software suite dfnWorks can be downloaded from <https://github.com/dfnWorks/dfnWorks-Version2.0>. Generation files for these simulations can be obtained by contacting the corresponding authors.

## References

- Barbier, E. (2002). Geothermal energy technology and current status: An overview. *Renewable & Sustainable Energy Reviews*, 6, 3–65.
- Berkowitz, B., & Balberg, I. (1993). Percolation theory and its application to groundwater hydrology. *Water Resources Research*, 29(4), 775–794.
- Berkowitz, B., & Scher, H. (1997). Anomalous transport in random fracture networks. *Physical Review Letters*, 79(20), 4038–4041.
- Berkowitz, B., & Scher, H. (1998). Theory of anomalous chemical transport in random fracture networks. *Physical Review E*, 57(5), 5858–5869.
- Bianchi, M., & Pedretti, D. (2017). Geological entropy and solute transport in heterogeneous porous media. *Water Resources Research*, 53, 4691–4708.
- Bonnet, E., Bour, O., Odling, N. E., Davy, P., Main, I., Cowie, P., et al. (2001). Scaling of fracture systems in geological media. *Reviews of Geophysics*, 39(3), 347–383.
- Cacas, M. C., Ledoux, E., De Marsily, G., Barbreau, A., Calmels, P., Gaillard, B., et al. (1990). Modeling fracture flow with a stochastic discrete fracture network: Calibration and validation. 2: The transport model. *Water Resources Research*, 26(3), 491–500.
- Comolli, A., & Dentz, M. (2017). Anomalous dispersion in correlated porous media: A coupled continuous time random walk approach. *European Physical Journal B*, 90(9), 166.
- Cvetkovic, V., Painter, S., Outters, N., & Selroos, J. (2004). Stochastic simulation of radionuclide migration in discretely fractured rock near the Äspö hard rock laboratory. *Water Resources Research*, 40, W02404. <https://doi.org/10.1029/2003WR002655>
- de Dreuzy, J.-R., Darcel, C., Davy, P., & Bour, O. (2004). Influence of spatial correlation of fracture centers on the permeability of two-dimensional fracture networks following a power law length distribution. *Water Resources Research*, 40, W01502. <https://doi.org/10.1029/2003WR002260>

- de Dreuz, J.-R., Méheust, Y., & Pichot, G. (2012). Influence of fracture scale heterogeneity on the flow properties of three-dimensional discrete fracture networks (dfn). *Journal of Geophysical Research*, 117, B11207. <https://doi.org/10.1029/2012JB009461>
- Demmy, G., Berglund, S., & Graham, W. (1999). Injection mode implications for solute transport in porous media: Analysis in a stochastic Lagrangian framework. *Water Resources Research*, 35(7), 1965–1973.
- Dentz, M., Kang, P. K., Comolli, A., Le Borgne, T., & Lester, D. R. (2016). Continuous time random walks for the evolution of Lagrangian velocities. *Physical Review Fluids*, 1(7), 074004.
- Dentz, M., Le Borgne, T., Englert, A., & Bijeljic, B. (2011). Mixing, spreading and reaction in heterogeneous media: A brief review. *Journal of Contaminant Hydrology*, 120–121, 1–17.
- Dershowitz, W. (2014). *FracMan version 7.4—Interactive discrete feature data analysis, geometric modeling, and exploration simulation: User documentation*. Redmond, Washington, DC: Golder, LLC. Retrieved from <http://fracman.golder.com/>
- Dershowitz, W., & Fidelibus, C. (1999). Derivation of equivalent pipe network analogues for three-dimensional discrete fracture networks by the boundary element method. *Water Resources Research*, 35(9), 2685–2691.
- Erhel, J., de Dreuz, J.-R., & Poirriez, B. (2009). Flow simulation in three-dimensional discrete fracture networks. *SIAM Journal on Scientific Computing*, 31(4), 2688–2705.
- Frampton, A., & Cvetkovic, V. (2009). Significance of injection modes and heterogeneity on spatial and temporal dispersion of advecting particles in two-dimensional discrete fracture networks. *Advances in Water Resources*, 32(5), 649–658.
- Gotovac, H., Cvetkovic, V., & Andricevic, R. (2009). Flow and travel time statistics in highly heterogeneous porous media. *Water Resources Research*, 45, W07402. <https://doi.org/10.1029/2008WR007168>
- Gotovac, H., Cvetkovic, V., & Andricevic, R. (2010). Significance of higher moments for complete characterization of the travel time probability density function in heterogeneous porous media using the maximum entropy principle. *Water Resources Research*, 46, W05502. <https://doi.org/10.1029/2009WR008220>
- Hagberg, A. A., Schult, D. A., & Swart, P. (2008). Exploring network structure, dynamics, and function using networkx. In *Proceedings of the 7th Python in Science Conferences (SciPy 2008)* (Vol. 2008, pp. 11–16). Pasadena, CA: SciPy Organizers.
- Huseby, O., Thovet, J. F., & Adler, P. M. (2001). Dispersion in three-dimensional fracture networks. *Physics of Fluids*, 13(3), 594–615.
- Hyman, J. D., Aldrich, G., Viswanathan, H., Makedonska, N., & Karra, S. (2016a). Fracture size and transmissivity correlations: Implications for transport simulations in sparse three-dimensional discrete fracture networks following a truncated power law distribution of fracture size. *Water Resources Research*, 52, 6472–6489.
- Hyman, J. D., Gable, C. W., Painter, S. L., & Makedonska, N. (2014). Conforming Delaunay triangulation of stochastically generated three dimensional discrete fracture networks: A feature rejection algorithm for meshing strategy. *SIAM Journal on Scientific Computing*, 36(4), A1871–A1894.
- Hyman, J. D., Hagberg, A., Srinivasan, G., Mohd-Yusof, J., & Viswanathan, H. S. (2017). Predictions of first passage times in sparse discrete fracture networks using graph-based reductions. *Physical Review E*, 96(1), 013304.
- Hyman, J. D., Jiménez-Martínez, J., Viswanathan, H. S., Carey, J. W., Porter, M. L., Rougier, E., et al. (2016b). Understanding hydraulic fracturing: A multi-scale problem. *Philosophical Transactions of the Royal Society A*, 374(2078), 20150426.
- Hyman, J. D., Karra, S., Makedonska, N., Gable, C. W., Painter, S. L., & Viswanathan, H. S. (2015a). dfnWorks: A discrete fracture network framework for modeling subsurface flow and transport. *Computers & Geosciences*, 84, 10–19.
- Hyman, J. D., Painter, S. L., Viswanathan, H., Makedonska, N., & Karra, S. (2015b). Influence of injection mode on transport properties in kilometer-scale three-dimensional discrete fracture networks. *Water Resources Research*, 51, 7289–7308.
- Janković, I., & Fiori, A. (2010). Analysis of the impact of injection mode in transport through strongly heterogeneous aquifers. *Advances in Water Resources*, 33(10), 1199–1205.
- Ji, S.-H., Park, Y.-J., & Lee, K.-K. (2011). Influence of fracture connectivity and characterization level on the uncertainty of the equivalent permeability in statistically conceptualized fracture networks. *Transport in Porous Media*, 87(2), 385–395.
- Jiménez-Martínez, J., Longuevergne, L., Borgne, T., Davy, P., Russian, A., & Bour, O. (2013). Temporal and spatial scaling of hydraulic response to recharge in fractured aquifers: Insights from a frequency domain analysis. *Water Resources Research*, 49, 3007–3023.
- Jiménez-Martínez, J., & Negre, C. F. A. (2017). Eigenvector centrality for geometric and topological characterization of porous media. *Physical Review E*, 96(1), 013310.
- Johnson, J., Brown, S., & Stockman, H. (2006). Fluid flow and mixing in rough-walled fracture intersections. *Journal of Geophysical Research*, 111, B12206. <https://doi.org/10.1029/2005JB004087>
- Journel, A. G., & Deutsch, C. V. (1993). Entropy and spatial disorder. *Mathematical Geosciences*, 25(3), 329–355.
- Kang, P. K., Brown, S., & Juanes, R. (2016). Emergence of anomalous transport in stressed rough fractures. *Earth and Planetary Science Letters*, 454, 46–54.
- Kang, P. K., Dentz, M., Le Borgne, T., & Juanes, R. (2015). Anomalous transport on regular fracture networks: Impact of conductivity heterogeneity and mixing at fracture intersections. *Physical Review E*, 92(2), 022148.
- Kang, P. K., Dentz, M., Borgne, T. L., Lee, S., & Juanes, R. (2017). Anomalous transport in disordered fracture networks: Spatial Markov model for dispersion with variable injection modes. *Advances in Water Resources*, 106, 80–94.
- Karrer, B., Newman, M. E., & Zdeborová, L. (2014). Percolation on sparse networks. *Physical Review Letters*, 113(20), 208–702.
- Kitanidis, P. K. (1994). The concept of the Dilution Index. *Water Resources Research*, 30(7), 2011–2026.
- Klint, K., Gravesen, P., Rosenbom, A., Laroche, C., Trenty, L., Lethiez, P., et al. (2004). Multi-scale characterization of fractured rocks used as a means for the realistic simulation of pollutant migration pathways in contaminated sites: A case study. *Water, Air, & Soil Pollution*, 4(4–5), 201–214.
- Kreft, A., & Zuber, A. (1978). On the physical meaning of the dispersion equation and its solutions for different initial and boundary conditions. *Chemical Engineering Science*, 33(11), 1471–1480.
- LaGrIT (2013). *Los Alamos Grid Toolbox (LaGrIT)*. Los Alamos, NM: Los Alamos National Laboratory. Retrieved from <http://lagrit.lanl.gov>
- Lichtner, P., Hammond, G., Lu, C., Karra, S., Bisht, G., Andre, B., Mills, R., & Kumar, J. (2015). *PFLOTRAN user manual: A massively parallel reactive flow and transport model for describing surface and subsurface processes* (Tech. Rep. LA-UR-15–20403). Los Alamos, NM: Los Alamos National Laboratory.
- Long, J., & Witherspoon, P. A. (1985). The relationship of the degree of interconnection to permeability in fracture networks. *Journal of Geophysical Research*, 90(B4), 3087–3098.
- Makedonska, N., Hyman, J. D., Karra, S., Painter, S. L., Gable, C. W., & Viswanathan, H. S. (2016). Evaluating the effect of internal aperture variability on transport in kilometer scale discrete fracture networks. *Advances in Water Resources*, 94, 486–497.
- Makedonska, N., Painter, S. L., Bui, Q. M., Gable, C. W., & Karra, S. (2015). Particle tracking approach for transport in three-dimensional discrete fracture networks. *Computational Geosciences*, 19(5), 1123–1137.

- Moreno, L., Tsang, Y. W., Tsang, C. F., Hale, F. V., & Neretnieks, I. (1988). Flow and tracer transport in a single fracture, a stochastic model and its relation to some field observations. *Water Resources Research*, 24(12), 2033–2048.
- Mustapha, H., & Mustapha, K. (2007). A new approach to simulating flow in discrete fracture networks with an optimized mesh. *SIAM Journal on Scientific Computing*, 29, 1439.
- Ottino, J. M. (1989). *The kinematics of mixing: Stretching, chaos, and transport*. Cambridge, UK: Cambridge University Press.
- Painter, S. L., Gable, C. W., & Kelkar, S. (2012). Pathline tracing on fully unstructured control-volume grids. *Computational Geosciences*, 16(4), 1125–1134.
- Park, Y.-J., Lee, K.-K., Kosakowski, G., & Berkowitz, B. (2003). Transport behavior in three-dimensional fracture intersections. *Water Resources Research*, 39(8), 1215. <https://doi.org/10.1029/2002WR001801>
- Pichot, G., Erhel, J., & de Dreuzy, J. (2010). A mixed hybrid mortar method for solving flow in discrete fracture networks. *Applicable Analysis*, 89(10), 1629–1643.
- Pichot, G., Erhel, J., & de Dreuzy, J. (2012). A generalized mixed hybrid mortar method for solving flow in stochastic discrete fracture networks. *SIAM Journal on Scientific Computing*, 34(1), B86–B105.
- Rhén, I. (1997). *Äspö HRL: Geoscientific evaluation 1997/4: Results from pre-investigations and detailed site characterization: Comparison of predictions and observations: Hydrology, groundwater chemistry and transport of solutes*. Stockholm, Sweden: Svensk kärnbränslehantering AB/Swedish Nuclear Fuel and Waste Management.
- Roques, C., Bour, O., Aquilina, L., & Dewandel, B. (2016). High-yielding aquifers in crystalline basement: Insights about the role of fault zones, exemplified by Armorican Massif, France. *Hydrogeological Journal*, 24(8), 2157–2170.
- Rubin, H., & Buddemeier, R. W. (1996). Transverse dispersion of contaminants in fractured permeable formations. *Journal of Hydrology*, 176(1), 133–151.
- Sanchez-Vila, X., Guadagnini, A., & Carrera, J. (2006). Representative hydraulic conductivities in saturated groundwater flow. *Reviews of Geophysics*, 44(3),
- Singhal, B. B. S., & Gupta, R. P. (2010). *Applied hydrogeology of fractured rocks*. Dordrecht, the Netherlands: Springer Science & Business Media.
- Svensk Kärnbränslehantering, A. B. (2010). *Data report for the safety assessment SR-site* (Tech. Rep. TR-10–52). Stockholm, Sweden: Svensk Kärnbränslehantering AB.
- Tsang, C. F., & Neretnieks, I. (1998). Flow channeling in heterogeneous fractured rocks. *Reviews of Geophysics*, 36(2), 275–298.
- Tsang, Y. W., & Tsang, C. F. (1989). Flow channeling in a single fracture as a two-dimensional strongly heterogeneous permeable medium. *Water Resources Research*, 25(9), 2076–2080.
- Tsang, Y. W., Tsang, C. F., Hale, F. V., & Dverstorp, B. (1996). Tracer transport in a stochastic continuum model of fractured media. *Water Resources Research*, 32(10), 3077–3092.
- Vanderborght, J., Mallants, D., & Feyen, J. (1998). Solute transport in a heterogeneous soil for boundary and initial conditions: Evaluation of first-order approximations. *Water Resources Research*, 34(12), 3255–3270.
- Willingham, T., Zhang, C., Werth, C. J., Valocchi, A. J., Oostrom, M., & Wietsma, T. W. (2010). Using dispersivity values to quantify the effects of pore-scale flow focusing on enhanced reaction along a transverse mixing zone. *Advances in Water Resources*, 33(4), 525–535.
- Wood, A. T. (1994). Simulation of the von Mises Fisher distribution. *Communications in Statistics*, 23(1), 157–164.